



Publication Year	2016
Acceptance in OA @INAF	2020-04-29T11:30:44Z
Title	Space Telescope and Optical Reverberation Mapping Project. IV. Anomalous Behavior of the Broad Ultraviolet Emission Lines in NGC 5548
Authors	Goad, M. R.; Korista, K. T.; De Rosa, G.; Kriss, G. A.; Edelson, R.; et al.
DOI	10.3847/0004-637X/824/1/11
Handle	http://hdl.handle.net/20.500.12386/24305
Journal	THE ASTROPHYSICAL JOURNAL
Number	824



SPACE TELESCOPE AND OPTICAL REVERBERATION MAPPING PROJECT. IV. ANOMALOUS BEHAVIOR OF THE BROAD ULTRAVIOLET EMISSION LINES IN NGC 5548

M. R. GOAD¹, K. T. KORISTA², G. DE ROSA^{3,4,5}, G. A. KRISS^{5,6}, R. EDELSON⁷, A. J. BARTH⁸, G. J. FERLAND⁹, C. S. KOCHANÉK^{3,4}, H. NETZER¹⁰, B. M. PETERSON^{3,4}, M. C. BENTZ¹¹, S. BISOGNI^{3,12}, D. M. CRENSHAW¹¹, K. D. DENNEY^{3,4,65}, J. ELY⁵, M. M. FAUSNAUGH³, C. J. GRIER^{13,14}, A. GUPTA³, K. D. HORNE¹⁵, J. KAASTRA^{16,17,18}, A. PANCOAST^{19,66}, L. PEI⁸, R. W. POGGE^{3,4}, A. SKIELBOE²⁰, D. STARKEY¹⁵, M. VESTERGAARD^{20,21}, Y. ZU²², M. D. ANDERSON¹¹, P. ARÉVALO²³, C. BAZHAW¹¹, G. A. BORMAN²⁴, T. A. BOROSON²⁵, M. C. BOTTORFF²⁶, W. N. BRANDT^{13,14,27}, A. A. BREEVELD²⁸, B. J. BREWER²⁹, E. M. CACKETT³⁰, M. T. CARINI³¹, K. V. CROXALL^{3,4}, E. DALLA BONTÀ^{32,33}, A. DE LORENZO-CÁCERES¹⁵, M. DIETRICH³⁴, N. V. EFIMOVA³⁵, P. A. EVANS¹, A. V. FILIPPENKO³⁶, K. FLATLAND³⁷, N. GEHRELS³⁸, S. GEIER^{39,40,41}, J. M. GELBORD^{42,43}, L. GONZALEZ³⁷, V. GORJIAN⁴⁴, D. GRUPE⁴⁵, P. B. HALL⁴⁶, S. HICKS³¹, D. HORENSTEIN¹¹, T. HUTCHISON²⁶, M. IM⁴⁷, J. J. JENSEN²⁰, M. D. JONER⁴⁸, J. JONES¹¹, S. KASPI^{10,49}, B. C. KELLY⁵⁰, J. A. KENNEA¹³, M. KIM⁵¹, S. C. KIM⁵¹, S. A. KLIMANOV³⁵, J. C. LEE⁵¹, D. C. LEONARD³⁷, P. LIRA⁵³, F. MACINNIS²⁶, E. R. MANNE-NICHOLAS¹¹, S. MATHUR^{3,4}, I. M. MCHARDY⁵⁴, C. MONTOURI⁵⁵, R. MUSSO²⁶, S. V. NAZAROV²⁴, R. P. NORRIS¹¹, J. A. NOUSEK¹³, D. N. OKHMAT²⁴, I. PAPADAKIS^{56,57}, J. R. PARKS¹¹, J.-U. POTT⁵⁸, S. E. RAFTER^{49,59}, H.-W. RIX⁵⁸, D. A. SAYLOR¹¹, J. S. SCHIMOIA⁶⁰, K. SCHNÜLLE⁵⁸, S. G. SERGEEV²⁴, M. SIEGEL¹³, M. SPENCER⁴⁸, H.-I. SUNG⁵¹, K. G. TEEMS¹¹, T. TREU^{50,61,67}, C. S. TURNER¹¹, P. UTTLEY⁶², C. VILLFORTH^{15,63}, Y. WEISS⁴⁹, J.-H. WOO⁴⁷, H. YAN⁶⁴, S. YOUNG⁷, AND W.-K. ZHENG³⁶

¹ University of Leicester, Department of Physics and Astronomy, Leicester, LE1 7RH, UK

² Department of Physics, Western Michigan University, 1120 Everett Tower, Kalamazoo, MI 49008-5252, USA

³ Department of Astronomy, The Ohio State University, 140 West 18th Avenue, Columbus, OH 43210, USA

⁴ Center for Cosmology and AstroParticle Physics, The Ohio State University, 191 West Woodruff Avenue, Columbus, OH 43210, USA

⁵ Space Telescope Science Institute, 3700 San Martin Drive, Baltimore, MD 21218, USA

⁶ Department of Physics and Astronomy, The Johns Hopkins University, Baltimore, MD 21218, USA

⁷ Department of Astronomy, University of Maryland, College Park, MD 20742-2421, USA

⁸ Department of Physics and Astronomy, 4129 Frederick Reines Hall, University of California, Irvine, CA 92697, USA

⁹ Department of Physics and Astronomy, The University of Kentucky, Lexington, KY 40506, USA

¹⁰ School of Physics and Astronomy, Raymond and Beverly Sackler Faculty of Exact Sciences, Tel Aviv University, Tel Aviv 69978, Israel

¹¹ Department of Physics and Astronomy, Georgia State University, 25 Park Place, Suite 605, Atlanta, GA 30303, USA

¹² Osservatorio Astrofisico di Arcetri, largo E. Fermi 5, I-50125, Firenze, Italy

¹³ Department of Astronomy and Astrophysics, Eberly College of Science, The Pennsylvania State University, 525 Davey Laboratory, University Park, PA 16802, USA

¹⁴ Institute for Gravitation and the Cosmos, The Pennsylvania State University, University Park, PA 16802, USA

¹⁵ SUPA Physics and Astronomy, University of St. Andrews, Fife, KY16 9SS Scotland, UK

¹⁶ SRON Netherlands Institute for Space Research, Sorbonnelaan 2, 3584 CA Utrecht, The Netherlands

¹⁷ Department of Physics and Astronomy, Universiteit Utrecht, P.O. Box 80000, 3508 Utrecht, The Netherlands

¹⁸ Leiden Observatory, Leiden University, P.O. Box 9513, 2300 RA Leiden, The Netherlands

¹⁹ Harvard-Smithsonian Center for Astrophysics, 60 Garden Street, Cambridge, MA 02138, USA

²⁰ Dark Cosmology Centre, Niels Bohr Institute, University of Copenhagen, Juliane Maries Vej 30, DK-2100 Copenhagen, Denmark

²¹ Steward Observatory, University of Arizona, 933 North Cherry Avenue, Tucson, AZ 85721, USA

²² Department of Physics, Carnegie Mellon University, 5000 Forbes Avenue, Pittsburgh, PA 15213, USA

²³ Instituto de Física y Astronomía, Facultad de Ciencias, Universidad de Valparaíso, Gran Bretaña N 1111, Playa Ancha, Valparaíso, Chile

²⁴ Crimean Astrophysical Observatory, P/O Nauchny, Crimea 298409, Russia

²⁵ Las Cumbres Global Telescope Network, 6740 Cortona Drive, Suite 102, Santa Barbara, CA 93117, USA

²⁶ Fountainwood Observatory, Department of Physics FJS 149, Southwestern University, 1011 East University Avenue, Georgetown, TX 78626, USA

²⁷ Department of Physics, The Pennsylvania State University, 104 Davey Lab, University Park, PA 16802, USA

²⁸ Mullard Space Science Laboratory, University College London, Holmbury St. Mary, Dorking, Surrey RH5 6NT, UK

²⁹ Department of Statistics, The University of Auckland, Private Bag 92019, Auckland 1142, New Zealand

³⁰ Department of Physics and Astronomy, Wayne State University, 666 West Hancock Street, Detroit, MI 48201, USA

³¹ Department of Physics and Astronomy, Western Kentucky University, 1906 College Heights Boulevard #11077, Bowling Green, KY 42101, USA

³² Dipartimento di Fisica e Astronomia "G. Galilei," Università di Padova, Vicolo dell'Osservatorio 3, I-35122 Padova, Italy

³³ INAF-Osservatorio Astronomico di Padova, Vicolo dell'Osservatorio 5 I-35122, Padova, Italy

³⁴ Department of Earth, Environment, and Physics, Worcester State University, 486 Chandler Street, Worcester, MA 01602, USA

³⁵ Pulkovo Observatory, 196140 St. Petersburg, Russia

³⁶ Department of Astronomy, University of California, Berkeley, CA 94720-3411, USA

³⁷ Department of Astronomy, San Diego State University, San Diego, CA 92182-1221, USA

³⁸ Astrophysics Science Division, NASA Goddard Space Flight Center, Greenbelt, MD 20771, USA

³⁹ Instituto de Astrofísica de Canarias, E-38200 La Laguna, Tenerife, Spain

⁴⁰ Departamento de Astrofísica, Universidad de La Laguna, E-38206 La Laguna, Tenerife, Spain

⁴¹ Gran Telescopio Canarias (GRANTECAN), E-38205 San Cristóbal de La Laguna, Tenerife, Spain

⁴² Spectral Sciences Inc., 4 Fourth Avenue, Burlington, MA 01803, USA

⁴³ Eureka Scientific Inc., 2452 Delmer Street, Suite 100, Oakland, CA 94602, USA

⁴⁴ MS 169-327, Jet Propulsion Laboratory, California Institute of Technology, 4800 Oak Grove Drive, Pasadena, CA 91109, USA

⁴⁵ Space Science Center, Morehead State University, 235 Martindale Drive, Morehead, KY 40351, USA

⁴⁶ Department of Physics and Astronomy, York University, Toronto, ON M3J 1P3, Canada

⁴⁷ Astronomy Program, Department of Physics & Astronomy, Seoul National University, Seoul, Korea

⁴⁸ Department of Physics and Astronomy, N283 ESC, Brigham Young University, Provo, UT 84602-4360, USA

⁴⁹ Physics Department, Technion, Haifa 32000, Israel

⁵⁰ Department of Physics, University of California, Santa Barbara, CA 93106, USA

⁵¹ Korea Astronomy and Space Science Institute, Korea

- ⁵² Astronomical Institute, St. Petersburg University, 198504 St. Petersburg, Russia
⁵³ Departamento de Astronomia, Universidad de Chile, Camino del Observatorio 1515, Santiago, Chile
⁵⁴ University of Southampton, Highfield, Southampton, SO17 1BJ, UK
⁵⁵ DiSAT, Università dell’Insubria, via Valleggio 11, I-22100, Como, Italy
⁵⁶ Department of Physics and Institute of Theoretical and Computational Physics, University of Crete, GR-71003 Heraklion, Greece
⁵⁷ IESL, Foundation for Research and Technology, GR-71110 Heraklion, Greece
⁵⁸ Max Planck Institut für Astronomie, Königstuhl 17, D-69117 Heidelberg, Germany
⁵⁹ Department of Physics, Faculty of Natural Sciences, University of Haifa, Haifa 31905, Israel
⁶⁰ Instituto de Física, Universidade Federal do Rio do Sul, Campus do Vale, Porto Alegre, Brazil
⁶¹ Department of Physics and Astronomy, University of California, Los Angeles, CA 90095-1547, USA
⁶² Astronomical Institute “Anton Pannekoek,” University of Amsterdam, Postbus 94249, NL-1090 GE Amsterdam, The Netherlands
⁶³ University of Bath, Department of Physics, Claverton Down, Bath BA2 7AY, UK
⁶⁴ Department of Physics and Astronomy, University of Missouri, Columbia, MO 65211, USA
Received 2016 February 1; accepted 2016 March 25; published 2016 June 3

ABSTRACT

During an intensive *Hubble Space Telescope* (*HST*) Cosmic Origins Spectrograph (COS) UV monitoring campaign of the Seyfert 1 galaxy NGC 5548 performed from 2014 February to July, the normally highly correlated far UV continuum and broad emission line variations decorrelated for ~ 60 – 70 days, starting ~ 75 days after the first *HST*/COS observation. Following this anomalous state, the flux and variability of the broad emission lines returned to a more normal state. This transient behavior, characterized by significant deficits in flux and equivalent width of the strong broad UV emission lines, is the first of its kind to be unambiguously identified in an active galactic nucleus reverberation mapping campaign. The largest corresponding emission line flux deficits occurred for the high ionization, collisionally excited lines C IV and Si IV(+O IV)], and also He II(+O III)], while the anomaly in Ly α was substantially smaller. This pattern of behavior indicates a depletion in the flux of photons with $E_{\text{ph}} > 54$ eV relative to those near 13.6 eV. We suggest two plausible mechanisms for the observed behavior: (i) temporary obscuration of the ionizing continuum incident upon broad line region (BLR) clouds by a moving veil of material lying between the inner accretion disk and inner (BLR), perhaps resulting from an episodic ejection of material from the disk, or (ii) a temporary change in the intrinsic ionizing continuum spectral energy distribution resulting in a deficit of ionizing photons with energies > 54 eV, possibly due to a transient restructuring of the Comptonizing atmosphere above the disk. Current evidence appears to favor the latter explanation.

Key words: galaxies: active – galaxies: individual (NGC – 5548) – galaxies: nuclei – galaxies: Seyfert

Supporting material: animation

1. INTRODUCTION

One of the most secure correlations in studies of active galactic nuclei (AGNs) is that found between the ultraviolet (UV)-optical continuum variations and the UV-optical broad emission line (BEL) variations. This simple relation is causal in nature. The UV-optical broad emission lines arise in high-density, fast-moving gas that is photoionized by an intense source of ionizing continuum radiation originating from a disk of material feeding the central supermassive black hole. Intrinsic variations in the incident ionizing continuum flux translate into correlated changes in the BEL strengths and their ratios. That an AGN’s observed UV/optical continuum variations closely track the largely unobservable driving continuum is demonstrated by the observed positive correlations between the flux variations in the emission lines and the observed UV/optical continuum. Positive correlations are also observed between the UV/optical and X-ray variations (Clavel et al. 1992; Marshall et al. 1997; Peterson et al. 2000; Uttley et al. 2003; Edelson et al. 2015 hereafter Paper II).

This ubiquitous property has proven extremely useful because the correlated continuum and emission line variations may be used to probe the spatial distribution and kinematics of the BEL gas, probing size scales (roughly a few microarcseconds) inaccessible via more conventional means. This technique, commonly referred to as reverberation mapping

(RM; see Blandford & McKee 1982), in its simplest form can reveal the characteristic “size” of the broad emission line region (BLR) for lines of very different ionization states and arising in gas with a wide range in density, thereby mapping out the density and ionization structure of the BLR. However, its real power manifests when the measured delays between the continuum and emission line variations are coupled with velocity information. Time-resolved spectroscopy can reveal not only the bulk motion of the line-emitting gas, but has been usefully exploited to measure the mass of the central black hole in ~ 60 AGNs (e.g., Kaspi et al. 2000, 2007; Peterson et al. 2002; Bentz et al. 2010a; Denney et al. 2010; Grier et al. 2012; Peterson 2014, and references therein; see also Bentz & Katz 2015 for a comprehensive list of RM sources).

RM is now a mature field. Notable improvements have been made in target selection, campaign design, and observing strategies. Coupled with new techniques developed to isolate the variable broad emission lines from contaminating components and major advances in methods for recovering the emission line response function, these have facilitated improved dynamical mass estimates for several AGNs (Denney et al. 2006, 2009b, 2010; Barth et al. 2011; Brewer et al. 2011; Zu et al. 2011, 2013a, 2013b; Pancoast et al. 2012, 2014; Bentz et al. 2014), as well as black hole mass determinations for possibly super-Eddington sources (Grier et al. 2012; Du et al. 2014, 2015; Wang et al. 2014; Hu et al. 2015), objects with purported slim disks and exhibiting a different mode of accretion. Significantly, RM campaigns are now producing velocity-delay maps of sufficient fidelity that the gas

⁶⁵ NSF Postdoctoral Research Fellow.

⁶⁶ Einstein Fellow.

⁶⁷ Packard Fellow.

spatial configuration and dynamics can be discerned (Denney et al. 2009a; Bentz et al. 2010b, 2010a; Skielboe et al. 2015).

In 2014, the AGN Space Telescope and Optical Reverberation Mapping (STORM) collaboration undertook the most intensive RM experiment to date. Awarded 179 orbits in Cycle 22 with *HST*/COS, the aim was to provide the first high-fidelity, velocity-resolved delay maps for the strong, broad UV emission lines in an AGN. The chosen target, NGC 5548, has a well documented history of correlated large amplitude continuum and BEL variations at both UV and optical wavelengths (Clavel et al. 1991; Korista et al. 1995; Peterson et al. 2002, and references therein). The *HST*/COS observations are presented by De Rosa et al. (2015, hereafter Paper I) and are of an unprecedented quality. These data were supported by photometric observations with *Swift* (Paper II), as well as by ground-based photometric (Fausnaugh et al. 2016, hereafter Paper III) and spectroscopic (L. Pei et al. 2016, in preparation; hereafter Paper V) observations.

This remarkable data set has revealed a number of interesting and unexpected results. Chief among these is a temporary breakdown in one of the fundamental tenets of RM. Approximately 75 days after the start of the *HST*/COS campaign, the continuum and emission line variations appeared to decorrelate. This transient phenomenon, characterized by a significant and anomalous depression in the BEL flux and a notable reduction in emission line variability lasting ~ 65 –70 days, is the subject of this investigation.

2. REVERBERATION MAPPING

The primary goal of RM is to use correlated continuum and BEL variations to solve the transfer equation

$$L(V, t) = \int_0^\infty \Psi(V, \tau) C(t - \tau) d\tau, \quad (1)$$

where $\Psi(V, \tau)$, the transfer function (or convolution kernel), maps the *driving* continuum light curve at earlier times $C(t - \tau)$ onto the observed emission line light curve $L(V, t)$ at the current epoch.

To eliminate nuisance background components (e.g., the host galaxy contribution to the UV/optical continuum bands and contaminating narrow emission line contributions), this equation has traditionally been solved in its linearized form

$$\Delta L(V, t) = \int_0^\infty \Psi'(V, \tau) \Delta C(t - \tau) d\tau, \quad (2)$$

where $\Delta L(V, t)$ and $\Delta C(t - \tau)$ represent the variable component of $L(V, t)$ and $C(t - \tau)$, respectively, relative to some average background value. Here, the quantity of interest is $\Psi'(V, \tau)$, the emission line “response function.” In general, $\Psi'(V, \tau) \neq \Psi(V, \tau)$.

Underpinning this simple relation, and a prerequisite for a successful RM campaign, is that the continuum and emission line variations are causally related. More specifically the basic assumptions of RM are as follows.

1. At the distance of the BLR, the driving continuum source appears point-like.

2. The ionizing continuum and emission line photons propagate freely at the speed of light—i.e., the BLR filling factor is small.
3. There exists a simple causal (though not necessarily linear) relation between the observed continuum and emission line variations.
4. The observed continuum variations, modulo some scale factor and temporal smoothing function, are a suitable proxy for the unobserved driving ionizing continuum variations.
5. The dominant timescale is the light crossing time.

Violation of any of these assumptions will impact our ability to recover $\Psi'(V, \tau)$. Fortunately, in *the vast majority of previous RM experiments*, these assumptions are broadly consistent with the data.

3. FOLLOWING THE ENERGY

3.1. Anomalous BEL Variations

The strongest evidence to date for the violation of one of the above assumptions (specifically assumption 4) appeared during the middle of the AGN STORM campaign, upon comparison of the UV continuum and BEL light curves (Paper I).⁶⁸ While the UV continuum and BEL variations were well correlated at the start and end of the *HST* observing campaign, they appeared to decorrelate starting approximately midway through the campaign. It was for this reason that a separate analysis was performed in Paper I on the data for the two halves of the campaign. We illustrate this in Figure 1(c), where we compare a modified version of the C iv BEL light curve (colored points) with the continuum light curve at 1157 Å. We use emission line light curves based on the *direct integrations* over the bulk of the broad emission line reported in Paper I, and modified as described below.

For C iv and all other emission lines, we have *shifted the entire emission line light curve* according to the measured delay between the emission line and the 1157 Å continuum band as determined for *the first 75 days* of the *HST* campaign. We assume that this delay provides an adequate description of the delay between the continuum and emission line variations for the latter half of the campaign. For the measured delays, we use the peak and centroid of the cross-correlation function (hereafter CCF; see Table 1). The CCF centroids are calculated over the range in delay for which the CCF coefficient exceeds 80% of the peak value. Uncertainties are estimated using the model-independent FR/RSS Monte Carlo method (Peterson et al. 1998), computing 1000 realizations of each light curve, assuming random sampling and full replacement. Next, we remove an estimate for contaminating narrow emission line flux (Table 1, column 4; based on measurements of low-flux state spectra of NGC 5548 first reported by Crenshaw et al. 1993; see also Goad & Koratkar 1998), and then rescale the emission line light curve to the mean continuum flux over the first 75 days of the *HST* campaign. Finally, we scale the emission line variability amplitude by dividing through by the measured responsivity for each line (Section 3.3 and Table 2, column 2). In so doing, the continuum and emission line

⁶⁸ The only anomalies reported to date have been attributed solely to changes in the continuum reprocessing efficiency of BLR clouds (e.g., Maoz et al. 1992; Sparke 1993; Grier et al. 2008). In these cases, while the line responsivity changed, the emission line and continuum variations remain significantly correlated.

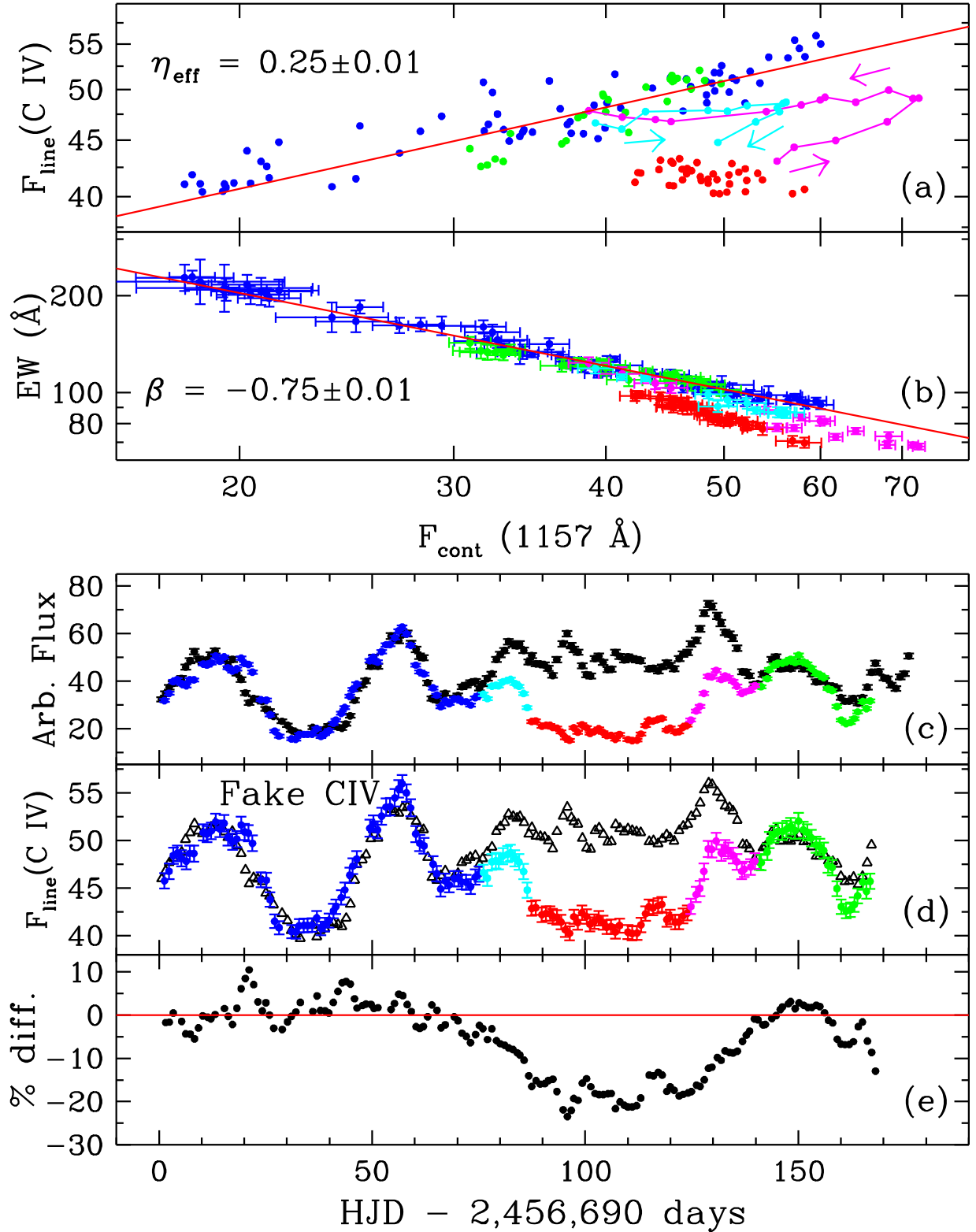


Figure 1. Upper two panels—(a) $F(\text{CIV})$ vs. $F_{\text{cont}}(1157 \text{ \AA})$ plotted on a logarithmic scale, color coded as follows: HJD–2,400,000: 56,691.2813–56,765.1133 (blue), 56,766.1094–56,776.3984 (cyan), 56,777.4336–56,813.9688 (red), 56,814.7891–56,829.8281 (magenta), 56,830.8242–56,856.8438 (green). Error bars have been omitted for clarity. In particular, note the island of red points lying away from the main relation, as well as the cyan and magenta points which trace a contiguous path to and from the main relation. The red line indicates the best-fit slope to the blue and green points only. (b) $\text{EW}(\text{C IV})$ vs. $F_{\text{cont}}(1157 \text{ \AA})$ plotted on a logarithmic scale. As above, the red line indicates the best-fit slope to the blue and green points only. Bottom three panels—(c) a comparison between the scaled and shifted version of the C IV emission line light curve (colored points) and the observed 1157 \AA continuum light curve (black points), highlighting the anomalous flux and response in this emission line midway through the campaign. (d) A comparison between the observed C IV emission line light curve (colored points) and the reconstructed emission line light curve (black triangles; see the text for details). (e) The estimated percentage deficit in the C IV flux.

(An animation of this figure is available.)

Table 1
BEL Delays and Adopted Narrow Emission Line Fluxes

Line ID	CCF(cent) (days)	CCF(lag) (days)	F(narrow) (10^{-13} erg s $^{-1}$ cm $^{-2}$)
Ly α	6.69 ± 0.41	6.41 ± 0.51	8.9
Si IV + O IV]	5.80 ± 0.58	5.86 ± 0.89	1.2
C IV	4.97 ± 0.39	4.95 ± 0.50	7.0
He II + O III]	2.42 ± 0.44	2.14 ± 0.58	1.2

Table 2
Time-averaged BEL Responsivities and the Slope of the Intrinsic Baldwin Effect

Line ID	η_{eff}	β
Ly α	0.30 ± 0.01	-0.73 ± 0.02
Si IV + O IV]	0.45 ± 0.01	-0.58 ± 0.03
C IV	0.25 ± 0.01	-0.75 ± 0.01
He II + O III]	0.58 ± 0.04	-0.48 ± 0.04

variations should then be of similar amplitude (they will be identical if the response function were simply a delta function shifted in time).

Figures 1(a)–(c) indicate that starting from day 75 (cyan points), the C IV flux relative to our proxy measure of the ionizing continuum flux drops significantly and then remains anomalously low for ~ 40 days (red points), before recovering (magenta points) and again showing normal correlated behavior (green points). Additionally, during the anomalous period (red points), the emission line variability amplitude, relative to the observed continuum variations, is also significantly suppressed. Similar behavior, though of varying strength, is seen for *all of the strong, broad UV emission lines* (Section 3.4), and is indicative of a dramatic decline in the continuum reprocessing efficiency of the line-emitting gas, as inferred by the observed continuum at 1157 Å. We have examined the 1989 IUE/SWP, LWP (Clavel et al. 1991) and 1993 HST/FOS (Korista et al. 1995) monitoring campaigns on NGC 5548 to look for similar effects and found none. To our knowledge, the AGN STORM campaign is the first for which a decorrelation between the observed UV continuum and UV BEL variations of such long duration has been reported.

3.2. BEL Responsivity and Reprocessing Efficiency

Significant changes in the continuum reprocessing efficiency of an emission line are best revealed through studying the emission line responsivity and/or equivalent width (EW). The time-averaged emission line responsivity η_{eff} is the power-law index relating the observed continuum, preferably the band closest in wavelength to the ionizing continuum, and BEL fluxes, F_{cont} and F_{line} :

$$F_{\text{line}} \propto F_{\text{cont}}^{\eta_{\text{eff}}} \quad (3)$$

The exponent η_{eff} is normally measured after first removing contaminating contributions from nonvariable background components (e.g., the narrow emission lines and starlight from the host galaxy), and after correcting for the mean delay between the continuum and emission line variations (Pogge & Peterson 1992; Gilbert & Peterson 2003; Goad et al. 2004), in order to minimize the effects of geometrical dilution. Alternatively, the emission line EW and the continuum may be

related by

$$\text{EW}_{\text{line}} \propto F_{\text{cont}}^{\beta}, \quad (4)$$

where $\beta = \eta_{\text{eff}} - 1$. The relationship between line responsivity and emission line EW is thus made clear. For a strictly linear (1:1) response, $\eta_{\text{eff}} = 1$, $\beta = 0$, and the emission line EW remains constant relative to the continuum flux variations. If $\eta_{\text{eff}} = 0$, the emission line does not respond to variations in the driving continuum. In general, $\eta_{\text{eff}} < 1$ for most emission lines (i.e., a nonlinear response), and hence $\beta < 0$. Thus, the majority of emission lines will show an intrinsic Baldwin effect (Kinney et al. 1990). The measured value of η_{eff} will also depend upon the reference continuum band (since the amplitudes of the continuum variations are larger at shorter wavelengths—e.g., Wamsteker et al. 1990; Clavel et al. 1991; Papers II and III) and the degree of geometrical dilution (Gilbert & Peterson 2003; Goad & Korista 2014, 2015).

3.3. Measuring η_{eff} and Identifying the Anomaly

For the continuum light curve against which the emission line delays and their responsivities will be measured, we use the HST continuum band measurements centered at 1157 Å (Paper I), as this is the wavelength band accessible with HST/COS that lies nearest to the driving ionizing continuum and has negligible host galaxy contamination.⁶⁹ For illustrative purposes, we focus on the strong, broad C IV emission line, but we treat all other emission lines in the same fashion. To measure η_{eff} , we follow the procedure of Goad et al. (2004). Using the delay-corrected BEL light curve, we reconstruct the continuum flux associated with the BEL flux at the current epoch by interpolation, adopting a weighted average of the two bracketing continuum points. The appropriate weights are derived from the first-order structure function of the continuum light curve (Kawaguchi et al. 1998; Paltani 1999; Goad et al. 2004). Continuum data associated with emission line data shifted to epochs before the start of the campaign are determined by a linear extrapolation. Emission line points beyond the end of the campaign can be determined in a similar fashion. We do not use these extrapolated points (either emission line or continuum) when measuring the time-averaged BEL responsivity η_{eff} , preferring instead to exclude these data from the analysis. Uncertainties in the reconstructed continuum and emission line points were determined from a structure function analysis of their respective light curves (for details, see Goad et al. 2004).

Having corrected the data for the mean delay $\langle \tau \rangle$, we then fit the relation

$$\log F_{\text{line}} = A + \eta_{\text{eff}} [\log F_{\text{cont}}(1157\text{Å})] \quad (5)$$

to points lying outside of the anomaly (blue and green points only), assuming uncertainties in both the ordinate and abscissa. For C IV, the best-fit slope gives $\eta_{\text{eff}} = 0.25 \pm 0.01$ (Figure 1(a), solid red line). In Table 2, column 2, we report the best-fit slopes for the time-averaged responsivity η_{eff} and their 1σ uncertainties for all of the broad emission lines reported in Paper I. Quoted values are the centroid and 1σ

⁶⁹ Relative to the driving ionizing continuum variations, the observed UV and optical continuum variations are of lower amplitude and smeared in time (e.g., Papers II and III), and may at some wavelengths be significantly contaminated by more slowly varying background components.

uncertainties determined from bootstrap resampling of the (corrected) light curves (10,000 realizations) with full replacement.

Figure 1(a) indicates that during the anomaly (epochs 75–140) there is a dramatic and uncorrelated reduction in the C IV emission line flux and response amplitude to continuum variations. Note in particular the island of red points well below the main $\log F_{\text{line}} - \log F_{\text{cont}}$ relation with $\eta_{\text{eff}} \approx 0$, indicating either (i) an absence of emission line response to continuum variations, or (ii) that the ionizing continuum responsible for driving the observed BEL variations varies less than the 1157 Å continuum. Also, note that the journey away from the main relation (cyan points) into the anomaly forms a continuous path (as indicated by the cyan arrows). Curiously, when exiting the anomaly (magenta points), the data follow a similar path but in the reverse direction (magenta arrows) before rejoining the normal $F_{\text{line}} - F_{\text{cont}}$ behavior.⁷⁰ There are indications that the $\log F_{\text{line}} - \log F_{\text{cont}}$ relation is somewhat steeper at the end of the campaign (green points) than during the first 75 days (blue points), though some of this effect may result from the use of a single lag when correcting for the continuum emission line delays. Larger emission line responsivities (η_{eff}) are usually associated with the emergence from lower ionizing continuum flux states (Korista & Goad 2004; Goad & Korista 2014, 2015).

Figure 1(b) illustrates the relationship between the 1157 Å continuum flux and C IV EW, referenced to the 1157 Å continuum. The best-fit slope in this relation (fitting to data on either side of the anomaly; i.e., blue and green points only) is $\beta = -0.75 \pm 0.01$, as expected since $\beta = \eta_{\text{eff}} - 1$. Once again, the color coded behavior described above is evident. There is an island of red points lying below the main relation and for which $\beta \approx -1$, while the cyan and magenta points taken together appear as extensions of the same relation with a slope intermediate between that of the main relation and that of the anomaly. The same general behavior, though differing in detail and with differing noise levels, is seen for Ly α , Si IV(+O IV)], and He II(+O III)].

3.4. Measuring the Amplitude of the Anomaly

In previous AGN RM campaigns, the strong positive correlation observed between the UV/optical continuum and BEL variations provides substantive supporting evidence that the UV and optical continuum variations are reasonable proxies, though smaller in amplitude and smeared in time, for the variable driving ionizing continuum. The strong positive correlation observed between the continuum and emission line variations pre- and post-anomaly for this campaign suggests that over these time periods the UV/optical continuum variations are also suitable proxies for the variable driving ionizing continuum. If this interpretation is correct, these data may then be used to infer the “expected” form of the emission line light curve during the anomaly—that is, as if the anomaly had not occurred.

Using the β values reported in Table 2, column 3, we reconstruct the emission line flux corresponding to the observed continuum flux at 1157 Å and shifted in time according to the delay reported in Table 1, column 2.⁷¹ In

Figure 1(d), we display a comparison between the observed (colored points) and reconstructed (black triangles) emission line light curve for C IV. In Figures 2(a)–(d), we show the observed (colored points) and reconstructed (black triangles) emission line light curves for all of the strong UV emission lines reported in Paper I, here normalized to their mean values over the first 75 days of the campaign. There are indications (e.g., Figures 2(a)–(d)) that the start times, stop times, and duration of the anomaly differs among the emission lines. If real, timing differences among the various lines may provide additional clues about the BLR structure. We defer investigation of this effect to a future paper.

Using the observed and reconstructed emission line light curves, we can measure the fraction of line emission lost f_{lost} during the period of the anomaly, $f_{\text{lost}} = [(f_{\text{rec}} - f_{\text{obs}})/f_{\text{rec}}] \times 100\%$ (e.g., Figure 1(e)), where f_{obs} and f_{rec} represent the observed and reconstructed emission line fluxes, respectively. We find time-averaged fractional losses of $\sim 23\%$ (Si IV(+O IV)], $\sim 21\%$ (He II(+O III)], $\sim 18\%$ (C IV), and $\sim 9\%$ (Ly α) during the time period spanning the anomaly. The largest flux deficit is found for Si IV and He II, followed closely by C IV, while Ly α shows the smallest (by a factor 2) flux deficit (Figures 2(a)–(d)). In Table 3, we report the measured time-averaged emission line EWs over the period spanning the anomaly (Figure 1(a)—red points) and compare it with the “expected” EW, here defined as the EW measured from the main relation (solid red line in Figure 1(b)) that corresponds to the average continuum level measured over the duration of the anomalous period [$F_{\text{cont}}(1157\text{Å}) = (4.84 \pm 0.37) \times 10^{-14} \text{ erg s}^{-1} \text{ cm}^{-2} \text{ Å}^{-1}$]. The measured deficit in EW is largest for Si IV(+O IV)] ($\sim 24\%$), followed by He II(+O III)] ($\sim 21\%$), C IV ($\sim 19\%$), and then Ly α ($\sim 11\%$), in good agreement with the estimates given above.

The analyzes described here and illustrated in Figures 1 and 2 can be further extended to include the strong optical recombination lines (Paper V, in preparation), and it may also be applied as a function of projected line of sight (LOS) velocity for all of the strong, broad UV and optical emission lines. In particular, it may be possible to see the effects of the transition into, through, and out of the anomaly in the velocity-resolved data, thereby constraining the BLR geometry and dynamics. This will require the highest fidelity light curves, free from contaminating narrow absorption and emission lines. These are typically obtained from spectral decomposition of the emission lines and is work in progress. Finally, we note that any variability in the EWs of the weak absorption lines associated with the outflow is unrelated to the anomaly, as clearly indicated by the fact that He II(+O III)] is strongly affected by the anomaly but has no absorption lines.

4. DISCUSSION

The observed behavior of the broad emission lines during the middle of the *HST*/COS campaign is consistent with a temporary yet significant softening of the ionizing continuum spectral energy distribution (SED) incident upon the BLR lasting ~ 40 days (Figure 1, red points). The cyan and magenta points may represent transition phases (each lasting ~ 1 –2 weeks) straddling the anomalous period. In the following, we suggest two plausible scenarios to account for the anomalous behavior of the broad emission lines.

⁷⁰ An animated GIF of this behavior is available in the online material.

⁷¹ A more thorough treatment would instead solve for the transfer function using those epochs bracketing the anomaly, and then apply forward modeling to infer the expected emission line fluxes during the anomalous period. This will be explored in the future but is beyond the scope of the current work.

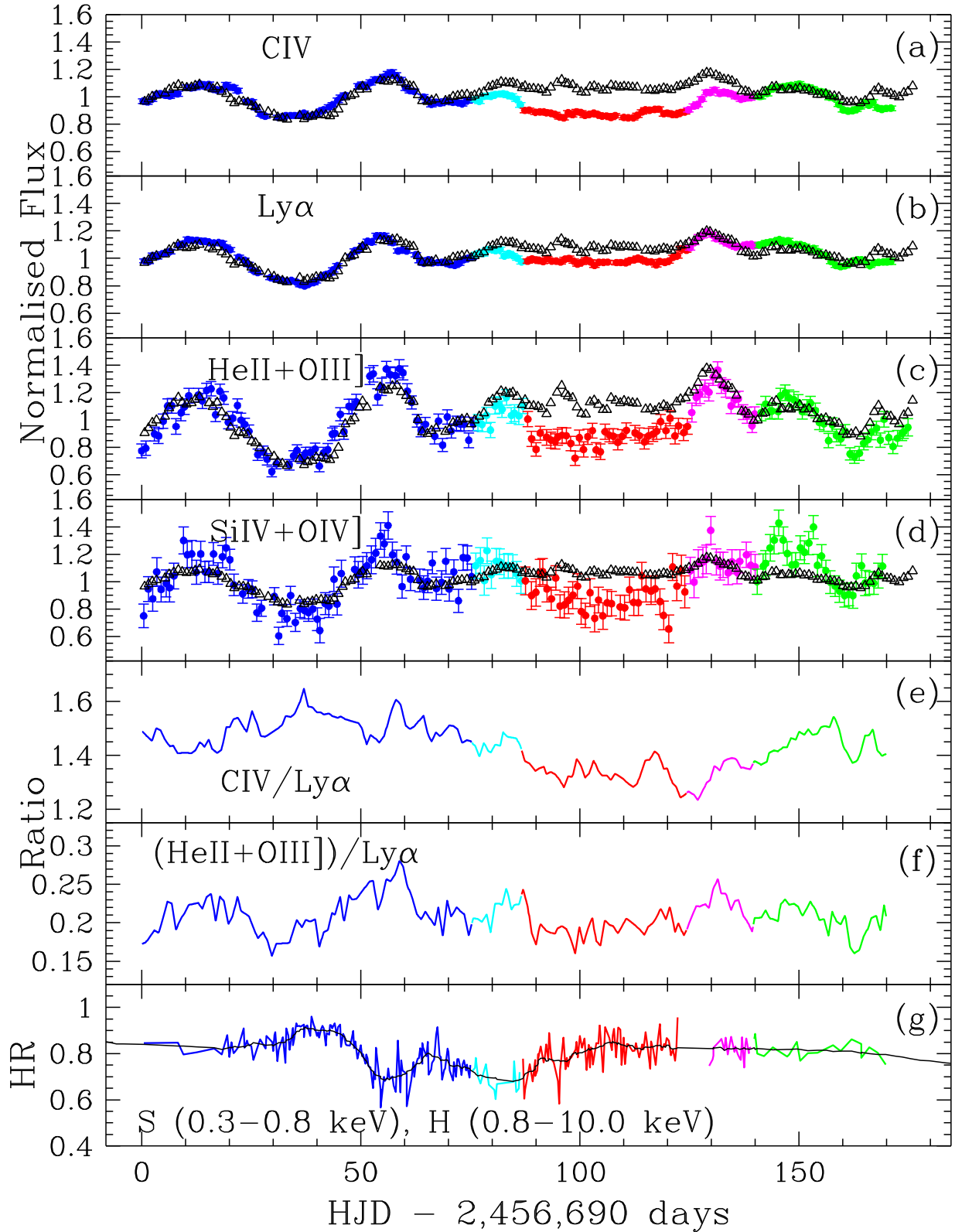


Figure 2. Panels (a)–(d): a comparison between the observed BEL light curves (color coded as described in the text) and their respective *reconstructed* light curves (black triangles). Each has been shifted backward in time according to the measured delay between the 1157 Å continuum and emission line light curve for that particular line, determined over the first 75 days. Panels (e)–(f): time-variable emission line ratios $C\text{ IV}/Ly\alpha$ and $(He\text{ II}+O\text{ III}]/Ly\alpha$. (g) The time-variable *Swift*/XRT X-ray hardness ratio ($H-S/(H+S)$) color coded as above. The solid black line indicates the hardness ratio after smoothing with a 15 point boxcar filter.

In Figure 2(e), we show the light curve for a powerful diagnostic BEL flux ratio involving the two strongest emission lines, $C\text{ IV}/Ly\alpha$ (e.g., Netzer 1990; Shields et al. 1995). This

temperature-sensitive ratio is a measure of the heating-cooling balance within the BEL clouds, centered on the average ionizing photon energy of ~ 100 eV, estimated for the central

Table 3
Time-averaged BEL EWs for the Anomaly and the Main Relation

Line ID	EW (Å) (anomaly)	EW (Å) (main relation)
Ly α	64.5 \pm 5.1	72.5 \pm 5.9
Si IV + O IV]	6.2 \pm 0.9	8.2 \pm 1.2
C IV	86.2 \pm 6.9	106.3 \pm 8.3
He II + O III]	12.5 \pm 1.3	15.9 \pm 3.3

Note. The EWs are here measured with respect to the average UV continuum flux at 1157 Å for those epochs spanning the time of the anomaly (Figure 1(a) —red points); $F_{\text{cont}}(1157 \text{ Å}) = (4.84 \pm 0.37) \times 10^{-14} \text{ erg s}^{-1} \text{ cm}^{-2} \text{ Å}^{-1}$.

source in NGC 5548 (Medhipour et al. 2015). This flux ratio is thus particularly sensitive to the SED of the incident ionizing continuum.⁷² During the first ~ 80 days, the C IV/Ly α flux ratio varies (weakly) inversely with the continuum variability, owing to the somewhat larger responsivity of Ly α (Table 2, column 2). Approximately coincident with the onset of the anomaly, this emission line flux ratio then exhibits a gradual decline, and continues to decline (on average) for the duration of the anomalous period before eventually rising again as the source behavior returns to normal.

We also show in Figure 2(f) the light curve for the BEL flux ratio, He II(+O III)]/Ly α . This flux ratio is sensitive to the ratio of photons responsible for ionizing the He⁺ ion ($E_{\text{ph}} > 54.4 \text{ eV}$) to those responsible for ionizing hydrogen ($E_{\text{ph}} > 13.6 \text{ eV}$). During the first ~ 87 days, this flux ratio correlates directly with the observed continuum variations, owing to the substantially larger responsivity in He II when compared to Ly α . It then quickly drops and remains approximately constant throughout the anomalous period. This behavior is indicative of a reduction in the incident flux of photons capable of ionizing He⁺ relative to the flux of photons responsible for ionizing hydrogen over the time period of anomalous emission line behavior. We note that the time-dependent behavior of this pair of BEL flux ratios is also reflected in the comparison of panels (a)–(c) of Figure 2.

Contemporaneous observations in the soft (0.3–0.8 keV) and hard (0.8–10 keV) X-ray bands with *Swift*/XRT (Figure 1 in Paper II) indicate a gradual decline in the soft and hard X-ray photon fluxes starting around day 75 (the onset of the anomaly), beyond which the measured flux in the observed UV continuum bands is trending upward. In Figure 2(g), we show the hardness ratio, $\text{HR} = (\text{H} - \text{S})/(\text{H} + \text{S})$, constructed from the soft (S) and hard (H) X-ray bands as defined in Paper II (see also Medhipour et al. 2016). Figure 2(g) indicates that on entering the anomalous period the X-ray HR initially increases, thereafter remaining approximately constant with an average value similar to that measured at the start and end of the campaign. That is, there appears to be nothing unusual about the HR during the anomalous period. In general, the HR shows a marginal trend downward over the course of the campaign interrupted by two significant drops (indicative of a softer spectrum), starting ~ 50 days prior to the onset of the anomaly and lasting a combined total of ~ 60 days before returning to the more general trend. It is unclear whether these large excursions in HR prior to the anomaly are in any way

related to the anomaly. Significantly, we see no color-dependent changes in the UV-optical continuum band during the time of the anomaly.

On exiting the anomaly, the soft and hard X-ray photon fluxes appear to trend upward, coincident with the increasing trend in the C IV/Ly α flux ratio. While some of the observed X-ray variability is likely caused by changes in the absorption of X-ray photons in out-flowing material lying along our LOS (Kaastra et al. 2014), these data are also consistent with a gradual softening of the X-ray–UV continuum, notably in our LOS.

All of these observed temporal behaviors are consistent with a temporary yet significant softening of the incident ionizing continuum both along our LOS and toward the BLR. The larger emission line flux and EW deficits exhibited by the collisionally excited lines (C IV and Si IV(+O IV)) are consistent with a drop in electron temperature that accompanied the softening of the ionizing SED. Together with the larger deficit in the broad He II emission line compared to Ly α , the evidence points to most of the softening occurring for $E_{\text{ph}} > 54 \text{ eV}$.

We suggest two mechanisms to explain the temporary softening of the incident ionizing continuum.

- i. A temporary obscuration of the ionizing continuum source incident upon BLR clouds by a moving veil of gas lying between the inner accretion disk and the inner BLR. This could represent an episodic ejection of material from the accretion disk. This veiling gas should be moderately highly ionized and of modest column density to produce the phenomena described above. These details are left for future investigation.
- ii. A temporary change in the intrinsic ionizing SED leading to a reduction in the number of ionizing photons, particularly above $\sim 54 \text{ eV}$. NGC 5548 apparently has a hard ionizing continuum, in which Comptonization plays an important role (Magdziarz et al. 1998; Medhipour et al. 2015). A temporary restructuring of the Comptonizing atmosphere situated above the inner accretion disk could significantly reduce the production of EUV continuum photons.

Since all of the broad emission lines (UV and optical) display a deficit in flux during the anomaly, then if temporary obscuration is the mechanism responsible, this imposes constraints on the nature of the obscuring veil of material and/or the BLR geometry. For example, for the obscuring veil of material to affect all lines simultaneously, it must cover a large solid angle, thus constraining its location to be close to the continuum source. Alternatively, if the BLR is in a flattened configuration, the obscuring veil of material need not be raised to very large scale-heights above the disk in order to affect all of the emission lines simultaneously, though such configurations for the BLR may be precluded on energetic grounds. Indeed, it may even be possible to distinguish between these differing scenarios by investigating the variation in the start and end times of the anomalous behavior among different lines.

Evidence for a change in the disk geometry can be found in high-resolution *Chandra* and *XMM-Newton* X-ray spectra of NGC 5548 taken during 2013–2014 (Di Gesu et al. 2015; Medhipour et al. 2016). Based on an observed reduction in the covering fraction of the X-ray obscurer at higher source

⁷² In the absence of changes in the ionizing SED, variations in the delay-corrected emission line flux ratios are mainly due to intrinsic differences between their individual line responsivities, and any remaining residual reverberation effects (e.g., geometrical dilution).

luminosities, Di Gesu et al. (2015) and Mehdipour et al. (2016) argue that the continuum-emitting region producing the soft excess becomes larger as the source brightens. If this brightening coincides with a puffing up of a disk whose outer regions are optically thick at photon energies $E_{\text{ph}} > 54$ eV, then this gas may provide the shielding necessary to explain the observations.

However, while obscuration can plausibly explain the significant drop in flux and EW of the broad emission lines during the anomaly, it does not readily explain their reduced amplitude of variability. While an obscuring screen of material will reduce the flux of ionizing continuum photons incident upon BLR clouds, the fractional variability amplitude of the continuum will remain unchanged. By contrast, physical changes in the Comptonizing atmosphere altering the SED at especially EUV photon energies might also lead naturally to suppressed variability at these energies. The second scenario can thereby explain not only the significant emission line flux deficits, but also the absence of significant emission line variations ($\eta_{\text{eff}} \approx 0$) during the anomalous period. Note that our emission line reconstructions (Figures 2(a)–(d)) indicate that if the ionizing continuum had varied as the 1157 Å continuum did, we would have easily detected the corresponding emission line variations. In addition, the first scenario might be expected to be accompanied by a significant increase in the X-ray HR, with greater photoabsorption occurring for $E_{\text{ph}} < 1$ keV, while observations indicate that for the majority of the anomalous period the HR remains approximately constant (Figure 2(g)). On the other hand, a reorganization of the Comptonizing atmosphere could manifest itself differently. Speculating further, the decline in the variability amplitude of the 1157 Å continuum during days ~ 75 –120 resembles a damped oscillation, and could be a manifestation of a redistribution of energy within the Comptonizing atmosphere. A more detailed analysis of the *HST*/COS data and contemporaneous X-ray spectroscopy from *Chandra* and *Swift* (S. Mathur et al. 2016, in preparation) are currently underway. When combined, such data could potentially distinguish these (and possibly other) scenarios, thereby leading to a deeper understanding of the inner workings of AGN accretion disks.

From the outset of AGN STORM, we had assumed that correlated continuum and emission line variations were the primary (and perhaps only) means of probing the spatial distribution and kinematics of the BLR and the nature of the central engine. Instead, by good fortune, the presence of the anomaly, far from compromising the current RM campaign, has provided a different and rather unique window into the behavior of the central engine and the processes that drive the continuum and BEL variations.

5. SUMMARY

Analysis of the time-dependent behavior of the BEL reprocessing efficiency has proven to be a powerful tool for investigating the relationship between the ionizing continuum source and line-emitting gas. Here we have used it to reveal the origin of the anomalous behavior exhibited by the strong, broad UV emission lines during the middle of the 2014 *HST*/COS monitoring campaign of the nearby Seyfert 1 galaxy NGC 5548: a significant yet temporary softening of the ionizing continuum incident upon BLR clouds. By following the energy, we are able to recover the form for the expected emission line light curve during the anomaly, as though the

anomaly had not occurred. In so doing, we identified a potential route for utilizing all of the available data from this campaign in future attempts at recovering the emission line response function for the strongest broad UV emission lines.

Finally, we note that effects of this nature have been looked for, but not found, in previous UV spectroscopic monitoring campaigns of NGC 5548. At the level at which these effects are present in the 2014 *HST* campaign, they would have easily been detected if present in both the 1989 and 1993 UV monitoring campaigns on NGC 5548. We also do not find such behavior in the far more extensive 13 year optical monitoring data available for NGC 5548 (Gilbert & Peterson 2003; Goad et al. 2004). Thus, anomalous behavior of this kind is likely rare in this source. Since analyses similar to that presented here have yet to be performed on the archival UV and optical data sets available for other AGNs we are unable to comment on the occurrence rate of this phenomenon among RM AGNs.

Facility: *HST*(COS).

Support for *HST* program number GO-13330 was provided by NASA through a grant from the Space Telescope Science Institute, which is operated by the Association of Universities for Research in Astronomy, Inc., under NASA contract NAS5-26555. M.M.F., G.D.R., B.M.P., C.J.G., and R.W.P. are grateful for the support of the National Science Foundation (NSF) through grant AST-1008882 to The Ohio State University. A.J.B. and L.P. have been supported by NSF grant AST-1412693. A.V.F. and W.-K.Z. are grateful for financial assistance from NSF grant AST-1211916, the TABASGO Foundation, and the Christopher R. Redlich Fund. M.C. Bentz gratefully acknowledges support through NSF CAREER grant AST-1253702 to Georgia State University. M.C. Bottorff acknowledges HHMI for support through an undergraduate science education grant to Southwestern University. K.D.D. is supported by an NSF Fellowship awarded under grant AST-1302093. R.E. gratefully acknowledges support from NASA under awards NNX13AC26G, NNX13AC63G, and NNX13AE99G. J.M.G. gratefully acknowledges support from NASA under award NNX13CH61C. P.B.H. is supported by NSERC. K.D.H. acknowledges support from the UK Science and Technology Facilities Council through grant ST/J001651/1. M.I. acknowledges support from the Creative Initiative program, No. 2008-0060544, of the National Research Foundation of Korea (NRFK) funded by the Korean government (MSIP). M.D.J. acknowledges NSF grant AST0618209. S.R.O.N. is financially supported by NWO, the Netherlands Organization for Scientific Research. B.C.K. is partially supported by the UC Center for Galaxy Evolution. C.S.K. acknowledges the support of NSF grant AST-1009756. D.C.L. acknowledges support from NSF grants AST-1009571 and AST-1210311. P.L. acknowledges support from Fondecyt grant #1120328. A.P. acknowledges support from an NSF graduate fellowship and a UCSB Dean’s Fellowship. J.S.S. acknowledges CNPq, National Council for Scientific and Technological Development (Brazil) for partial support and The Ohio State University for warm hospitality. T.T. has been supported by NSF grant AST-1412315. T.T. and B.C.K. acknowledge support from the Packard Foundation in the form of a Packard Research Fellowship to T.T.; also, T.T. thanks the American Academy in Rome and the Observatory of Monteporzio Catone for kind hospitality. The Dark Cosmology Centre is funded by the Danish National Research Foundation.

M.V. gratefully acknowledges support from the Danish Council for Independent Research via grant No. DFF4002-00275. J.-H.W. acknowledges support by the National Research Foundation of Korea (NRF) grant funded by the Korean government (No. 2010-0027910). This research has made use of the NASA/IPAC Extragalactic Database (NED), which is operated by the Jet Propulsion Laboratory, California Institute of Technology, under contract with NASA.

REFERENCES

- Barth, A. J., Pancoast, A., Thorman, S. J., et al. 2011, *ApJ*, **743**, 4
- Bentz, M. C., Horenstein, D., Bazhaw, C., et al. 2014, *ApJ*, **796**, 8
- Bentz, M. C., Horne, K., Barth, A. J., et al. 2010a, *ApJ*, **720**, 46
- Bentz, M. C., & Katz, S. 2015, *PASP*, **127**, 67
- Bentz, M. C., Walsh, J. L., Barth, A. J., et al. 2010b, *ApJ*, **716**, 993
- Blandford, R. D., & McKee, C. F. 1982, *ApJ*, **255**, 419
- Brewer, B. J., Treu, T., Pancoast, A., et al. 2011, *ApJ*, **733**, 33
- Clavel, J., Nandra, K., Machino, F., et al. 1992, *ApJ*, **393**, 113
- Clavel, J., Reichert, G. A., Alloin, D., et al. 1991, *ApJ*, **366**, 64
- Crenshaw, M. D., Boggess, A., & Wu, C.-C. 1993, *ApJ*, **416**, 67
- Di Gesu, L., Constantini, E., Ebrero, J., et al. 2015, *A&A*, **579**, 42
- Denney, K. D., Bentz, M. C., Peterson, B. M., et al. 2006, *ApJ*, **653**, 152
- Denney, K. D., Peterson, B. M., Pogge, R. W., et al. 2009a, *ApJ*, **704**, 80
- Denney, K. D., Peterson, B. M., Pogge, R. W., et al. 2010, *ApJ*, **721**, 715
- Denney, K. D., Watson, L. C., Peterson, B. M., et al. 2009b, *ApJ*, **702**, 1353
- De Rosa, G., Peterson, B. M., Ely, J., et al. 2015, *ApJ*, **806**, 128 (Paper I)
- Du, P., Hu, C., Lu, K.-X., et al. 2014, *ApJ*, **782**, 45
- Du, P., Hu, C., Lu, K.-X., et al. 2015, *ApJ*, **806**, 22
- Edelson, R., Gelbord, J. M., Horne, K., et al. 2015, *ApJ*, **806**, 129 (Paper III)
- Fausnaugh, M. M., Denney, K. D., Barth, A. J., et al. 2015, arXiv:1510.05648, (Paper III)
- Fausnaugh, M. M., Denney, K. D., Barth, A. J., et al. 2016, *ApJ*, **821**, 56
- Gilbert, K. M., & Peterson, B. M. 2003, *ApJ*, **587**, 123
- Goad, M. R., & Korista, K. T. 2014, *MNRAS*, **444**, 43
- Goad, M. R., & Korista, K. T. 2015, *MNRAS*, **453**, 3662
- Goad, M. R., Korista, K. T., & Knigge, C. 2004, *MNRAS*, **352**, 277
- Grier, C. J., Peterson, B. M., Bentz, M. C., et al. 2008, *ApJ*, **688**, 837
- Grier, C. J., Peterson, B. M., Pogge, R. W., et al. 2012, *ApJ*, **755**, 60
- Hu, C., Du, P., & Lu, K.-X. 2015, *ApJ*, **804**, 138
- Kaasra, J. S., Kriss, G. A., Cappi, M., et al. 2014, *Science*, **345**, 64
- Kaspi, S., Brandt, W. N., Maoz, D., et al. 2007, *ApJ*, **659**, 997
- Kaspi, S., Smith, P. S., Netzer, H., et al. 2000, *ApJ*, **533**, 631
- Kinney, A. L., Rivo, A. R., & Koratkar, A. P. 1990, *ApJ*, **357**, 338
- Korista, K. T., Alloin, D., Barr, P., et al. 1995, *ApJS*, **97**, 285
- Korista, K. T., & Goad, M. R. 2004, *ApJ*, **606**, 749
- Kawaguchi, T., Mineshige, S., Umemura, M., & Turner, E. L. 1998, *ApJ*, **504**, 67
- Magdziarz, P., Blaes, O. M., Zdziarski, A. A., et al. 1998, *MNRAS*, **301**, 179
- Maoz, D. 1992, in *Physics of Active Galactic Nuclei*, ed. W. J. Duschl, & S. J. Wagner (Berlin: Springer), 214
- Marshall, H. L., Carone, T. E., Peterson, B. M., et al. 1997, *ApJ*, **479**, 222
- Medhipour, M., Kaasra, J. S., Kriss, G. A., et al. 2015, *A&A*, **575**, 22
- Mehdipour, M., Kaasra, J. S., Kriss, G. A., Cappi, M., Petrucci, P.-O., et al. 2016, *A&A*, **588**, 139
- Netzer, H., et al. 1990, in *Active Galactic Nuclei*, ed. R. D. Blandford et al. (Berlin: Springer), 57
- Paltani, S. 1999, *ASPC*, **159**, 293
- Pancoast, A., Brewer, B. J., & Treu, T. 2014, *MNRAS*, **455**, 3055
- Pancoast, A., Brewer, B. J., Treu, T., et al. 2012, *ApJ*, **754**, 49
- Peterson, B. M. 2014, *SSRv*, **183**, 253
- Peterson, B. M., Berlind, P., Bertram, R., et al. 2002, *ApJ*, **581**, 197
- Peterson, B. M., McHardy, I. M., Wilkes, B. J., et al. 2000, *ApJ*, **542**, 161
- Peterson, B. M., Wanders, I., Horne, K., et al. 1998, *PASP*, **110**, 660
- Pogge, R., & Peterson, B. M. 1992, *AJ*, **103**, 1084
- Shields, J. C., Ferland, G. J., & Peterson, B. M. 1995, *ApJ*, **441**, 507
- Sparke, L. S. 1993, *ApJ*, **404**, 570
- Skjelboe, A., Pancoast, A., Treu, T., et al. 2015, *MNRAS*, **454**, 144
- Uttley, P., Edelson, R., McHardy, I. M., et al. 2003, *ApJ*, **584**, 53
- Wamsteker, W., Rodriguez-Pascual, P., Wills, B. J., et al. 1990, *ApJ*, **354**, 446
- Wang, J.-M., Du, P., Hu, C., et al. 2014, *ApJ*, **793**, 108
- Zu, Y., Kochanek, C. S., Kozłowski, S., & Peterson, B. M. 2013a, arXiv:1310.6774
- Zu, Y., Kochanek, C. S., Kozłowski, S., & Udalski, A. 2013b, *ApJ*, **765**, 106
- Zu, Y., Kochanek, C. S., & Peterson, B. M. 2011, *ApJ*, **735**, 80